Highly efficient charge separation in model Z-scheme $TiO_2/TiSi_2/Si$ photoanode by micropatterned titanium silicide interlayer

M. Hannula[a], H. Ali-Löytty[a], K. Lahtonen[a], J. Saari[a], A. Tukiainen[b], M. Valden[a,*]

[a] *Surface Science Group, Laboratory of Photonics, Physics Unit, Tampere University, P.O. Box 692, FI-33014 Tampere, Finland*
[b] *Optoelectronics Research Centre, Laboratory of Photonics,Physics Unit, Tampere University, P.O. Box 692, FI-33014 Tampere, Finland*

Abstract

Atomic layer deposited (ALD) TiO_2 is an attractive material for improving the photoactivity and chemical stability of semiconductor electrodes in artificial photosynthesis. Using photoelectrochemical (PEC) measurements, we show that an interfacial, topographically microstructured $TiSi_2$ layer inside the TiO_2/Si heterojunction improves the charge carrier separation and shifts the water dissociation onset potential to more negative values. These observations are correlated with the X-ray photoelectron spectroscopy (XPS) and ultra-violet photoelectron spectroscopy (UPS) measurements, which reveal an increased band bending due to the $TiSi_2$ interlayer. Combined with the UV-Vis absorption results, the photoelectron spectroscopy measurements allow the reconstruction of the complete energy band diagram for the $TiO_2/TiSi_2/Si$ heterojunction and the calculation of the valence and conduction band offsets. The energy band alignment and improvements in PEC results reveal that the charge transfer across the heterojunction follows a Z-scheme model, where the metal-like $TiSi_2$ islands act as recombination centers at the interface.

Keywords: Titanium dioxide, Electronic band structure, Transition metal

*Corresponding author
Email address: mika.valden@tuni.fi (M. Valden)
URL: research.tuni.fi/surfsci/ (M. Valden)

silicides, X-ray photoelectron spectroscopy (XPS), Electrochemical characterization

1. Introduction

Converting solar energy directly into clean, easily storable hydrogen fuel has attracted a great deal of interest since its original discovery by Fujishima and Honda [1]. The method is based on photosynthetic water splitting, where semiconductor electrodes are used for photon absorption and charge transfer for enabling water oxidation and reduction [2]. A typical device consists of two electrodes: photoexcited holes are transferred to the photoanode for an oxygen evolution reaction (OER) and photoexcited electrons to the photocathode for a hydrogen evolution reaction (HER). Effective operation of the device requires that the photogenerated charge carriers (electron–hole pairs) can be separated efficiently and the charge transfer resistance can be minimized.

In recent years, especially TiO_2 has attracted tremendous research interest as both a photoactive and a protective layer on the surface of other small-band gap semiconductors such as Si, GaAs, and GaP. Especially the atomic layer deposited, electronically "leaky" TiO_2 has proven to be a very beneficial material for both OER and HER electrode coatings due to its electrical conductance and passivating properties [3, 4, 5, 6, 7]. However, the coupling between the TiO_2 overlayer and the semiconductor substrate requires careful interface engineering such that the charge transfer and the charge separation can be optimized. For example, on Si based electrodes the insulating SiO_2 native oxide at the interface can produce an excess barrier for charge transfer and cause a voltage loss across the heterojunction [8]. The problem has been mitigated, e.g., by depositing metallic Ti between the Si and TiO_2 layers immediately after cleaning the Si substrate from native oxide [5, 9]. Another option for improving the charge transfer across the heterojunction is to nanotexture the interface [10]. Also the charge separation capabilities, i.e. band bending, have been studied extensively [4, 11, 8]. For example Perego et al. [12] have measured how different

interlayer materials at the TiO_2/Si interface affect the band alignment of the heterojunction.

Also the Schottky barrier formation at the transition metal silicide/Si interface in general has attracted a lot of interest [13, 14, 15, 16, 17, 18]. Different models have related the barrier properties, for example, to the phase stoichiometry and structure [13], the chemical interactions at the interface [14] or heat of formation [15]. However, the results have often been contradictory with only a few details of the silicide fabrication process, layer thickness or oxide impurities and how they may affect the energy band structure. Additionally, lateral nano- or micro-scale variations in the interface structure produce further anomalies as the electric field gets pinched off inside the silicide structures, as analytically predicted by Tung [19, 20] and later verified by e.g. Rossi et al. [21, 22].

In this study, a micropatterned, laterally inhomogeneous $TiSi_2$ interlayer structure has been fabricated by thermally reducing a predeposited ALD grown TiO_2 film on an Si electrode into $TiSi_2$ followed by an ALD growth of a photoactive TiO_2 thin film onto the $TiSi_2$ layer. $TiSi_2$ has almost metal-like conductance, and due to the high temperature annealing in ultra-high vacuum, the insulating SiO_2 film can be removed between the Si and the $TiSi_2$ islands. Also, the properties of the $TiSi_2$ patterns can be adjusted by altering the thickness of the original TiO_2 interlayer before annealing. Furthermore, our photoelectrochemical measurements show that this affects the heterojunction band alignment and thus the onset potential for water splitting. We have used a combination of photoelectron spectroscopy (PES) and UV-Vis absorption spectroscopy to obtain complete understanding of the band energy diagram of the TiO_2/$TiSi_2$/Si heterojunction. The effects of the band alignment modifications have been verified by photoelectrochemistry (PEC) and surface photovoltage (SPV) measurements. The results show that an ultra-thin $TiSi_2$ interlayer induces a significant improvement (decrease) on the onset potential for photoelectrochemical water oxidation. The band alignment studies clearly show that the charge transfer follows the Z-scheme mechanism [23, 24, 25, 26, 27], where the interlayer acts as a charge recombination region.

2. Materials and methods

The P-doped (resistivity 1–20 Ω·cm) n-type Si(100) wafers were purchased from Wafer World, Inc. (Florida, USA). The 400 µm thick, 3 in. diameter prepolished wafers had been cut in the (100) orientation with a ± 1° accuracy. For the experiments 10×10 mm^2 squares were cleaved. The Si substrates were first cleaned by sonicating them for 45 min in 99.5% EtOH followed by a combination of annealing and atomic hydrogen treatments in UHV. The details of the UHV cleaning procedure are described in Ref. [28]. In short, the samples were first annealed to 1000 °C to remove native oxide. After this they were exposed to atomic hydrogen at 800 °C (10 min) and 400 °C (10 min) at $p_H = 1.0 \times 10^{-7}$ mbar, which removed the segregated Cu and Ni impurities, respectively. In all stages the sample temperature was monitored with a pyrometer (Land Cyclops 160B) using an emissivity value of $\varepsilon = 0.60$. The pyrometer reading was calibrated against a type K thermocouple in a separate system. After annealing, the surface cleanness and structure were verified by X-ray photoelectron spectroscopy and low energy electron diffraction (LEED) (See Refs [28, 29]). After the UHV cleaning, the samples were cooled down in UHV and transferred to the ALD system through the atmosphere. The exposure to air was kept less than 5 min.

2.1. Atomic layer deposition

The ALD deposition of TiO_2 was carried out using a Picosun Sunale ALD R200 Advanced reactor. Tetrakis(dimethylamido)titanium(IV) ($Ti(N(CH_3)_2)_4$, TDMAT, 99%, Strem Chemicals Inc., France), deionized water, and Ar (99.9999%, Oy AGA Ab, Finland) were used as the Ti precursor, O precursor, and carrier/purge/venting gas, respectively. The film growth rate was calibrated by ellipsometry (Rudolph Auto EL III Ellipsometer, Rudolph Research Analytical). During the ALD, the Si substrate temperature was kept at 200 °C. The vapor pressure of the TDMAT was increased to 3.6 mbar by heating the precursor bubbler to 76 °C, and the precursor gas delivery line was heated to 85

°C to prevent condensation. The water bubbler was sustained at 18 °C by a Peltier element for stability control. The substrate temperature was stabilized for 30 min before starting the deposition. The 200 °C ALD growth temperature was selected because it results in an amorphous growth whereas higher ALD temperatures produce strongly crystallized anatase TiO_2 [30, 31]. On the other hand, much lower substrate temperature would result in an incomplete precursor dissociation leading to higher remnant impurity concentrations, especially nitrogen from TDMAT. Low temperature deposition also produces more stoichiometric TiO_2 which, based on our previous research, cannot be modified by the post-treatments as effectively as the films grown at 200 °C [29].

Three separate depositions were conducted for each $TiO_2/TiSi_2/Si$ sample: (1) a 3, 10, or 30 nm thick film (84, 280, or 804 ALD cycles, respectively), which was converted into $TiSi_2$ by post annealing, (2) a 3 nm thick film was deposited on top of the previous $TiSi_2$ interlayer to enable interface analysis by XPS and UPS, and (3) finally a 27 nm film was deposited to reach a total TiO_2 film thickness of 30 nm, which is shown to be practical for PEC applications. Additionally, a control sample without any $TiSi_2$ interlayer (i.e. without step 1) was grown. After each ALD deposition step the samples were cooled down in nitrogen gas before transferring them back to UHV for post-treatments and photoelectron spectroscopy (PES) measurements. The exposure to ambient atmosphere during the transfer was approximately 5 min.

2.2. Formation of the $TiSi_2$ island structure

The post-annealing for converting TiO_2 film into $TiSi_2$ was performed in the preparation chamber of the NanoESCA spectromicroscopy system (Omicron NanoTechnology GmbH) [32]. The sample was annealed at 950 °C for 10 min. The heating setup consisted of a resistive PBN-heating element mounted to a manipulator close to the backside of the sample and the sample held in a Mo sample plate. The temperature was increased to the target value in approximately five minutes and monitored with a pyrometer. After the annealing the sample was transferred to the analysis chamber under UHV conditions for PES

measurements.

2.3. Photoelectron spectroscopy

The PES measurements were conducted in the analysis chamber of the NanoESCA system with a base pressure below 1×10^{-10} mbar. Focused monochromatized Al Kα radiation ($h\nu$ = 1486.5 eV) was utilized for core level XPS whereas valence band UPS spectra were measured with a focused nonmonochromatized He Iα radiation ($h\nu$ = 21.22 eV) using HIS 13 VUV Source (Focus GmbH). Under the normal operation mode the the X-ray source produces 36 W (12 kV $\times$ 3 mA) of emission power. In some cases this induced measurable surface photovoltages (SPV) ($\leq$ 0.15 eV) on the studied samples thus distorting the band position measurements [33]. To compensate this, the Si 2p spectra were measured also with 6 W X-ray power and the true band positions were deduced from these two measurements. Similar compensation was made for He Iα induced SPV by comparing the X-ray excited Si 2p core level position with and without He Iα radiation.

The XPS and UPS spectra were collected at the 0° takeoff angle with a photoemission electron microscope (PEEM) paired with a double hemispherical energy analyzer. The spectroscopic data was collected with only one hemisphere and a channeltron detector. For energy filtered imaging the second hemisphere was connected in series with the first one and the data was collected with a full field 2D multichannel plate detector. The energy resolution of the analyzer was set to 400 meV (pass energy 100 eV, slit 1 µm) and 100 meV (pass energy 50 eV, slit 0.5 µm) for XPS and UPS, respectively. In the spectroscopic mode the analysis area was set to 230 µm in diameter for XPS and 95 µm for UPS, corresponding to the maximum spot sizes of the radiation sources. Large analysis areas ensured that the results represent the average surface composition. In imaging mode the FoV was reduced to 35 µm to obtain better spatial resolution.

The chemical states of the elements were determined from the core level XP spectra by least-squares fitting of asymmetric Gaussian–Lorentzian line shapes after subtracting a Shirley type background. The analysis was made

in CasaXPS software version 2.3.17PR1.1 [34] using the Scofield photoionization cross-sections as relative sensitivity factors. The valence band maximum (VBM) and work function (WF) values were analyzed from UPS spectra and energy filtered image stacks. The value for the VBM was determined as the intersection between the background and the linear portion of the valence band leading edge and finally shifted 0.10 eV to a higher binding energy due to the analyzer related broadening, as measured on an Ag(111) reference sample. Similarly, the WF value was determined as the intersection between the background and the linear portion of the secondary electron cutoff edge. The WF value was corrected for the Schottky effect by shifting them to 98 meV higher energy [35]. The binding energy (E_b) scale of the energy analyzer was calibrated by setting the Ag(111) single crystal VBM to 0 eV.

2.4. Photoelectrochemical analysis

In order to improve the stability of the ALD deposited amorphous TiO_2 film against alkaline PEC conditions the samples used for the PEC measurements were annealed in a tube furnace in air at 400 °C for 45 min [29, 36]. The heat treatment induced crystallization of amorphous TiO_2 into rutile TiO_2 with a band gap of 3.2 eV [36]. After this the photoelectrochemical performance was studied in a homemade PEC cell (PTFE body, volume 3.5 cm^3), using a three-electrode system controlled by the Autolab PGSTAT12 potentiostat (Metrohm AG). The PEC tests ere conducted for the same four samples that were used in the PES measurements. This approach allowed us one-to-one correlation between the PES and PEC results. First, the back side of the samples was gently ground using a diamond file, and then the samples were inserted between a rubber O-ring and a stainless steel plate. The steel plate on the back side provided the electrical contact and the O ring ensured a well defined 0.28 cm^2 planar projected electrode surface area. An Ag/AgCl electrode (Leak-Free LF-2, Warner Instruments, LLC) and a Pt wire (surface area 0.82 cm^2) were used as reference and counter electrodes, respectively, in an aqueous solution of 1 M NaOH (pH = 13.6). The potential values were converted to the reversible

hydrogen electrode (RHE) scale by the equation $V_{\mathrm{RHE}} = V_{\mathrm{Ag/AgCl}} + 0.197\ \mathrm{V} + \mathrm{pH} \times 0.059\ \mathrm{V}$. Simulated solar spectrum was produced with a HAL-C100 solar simulator (Asahi Spectra Co., Ltd., JIS Class A at 400–1100 nm with AM1.5G filter) and the intensity was adjusted to 1.00 Sun using a 1 sun checker (model CS-30, Asahi Spectra Co., Ltd.). The photon flux was directed to the sample front surface through a 5 mm thick quartz glass window and a 18 mm thick electrolyte layer.

A unified PEC test program containing all the procedures was applied to test the samples using Nova 1.11 software. The PEC testing was started after a 10 min stabilization time by electrochemical impedance spectroscopy (EIS) at the open circuit potential (OCP) in dark with a frequency range from 0.1 Hz to 43 kHz. Then, the sample was subjected to a chopped light OCP measurement. Finally, a linear scan voltammetry (LSV) measurement was performed at 50 mV/s between the OCP and 2.0 V vs. RHE. Three potential scans were performed in the following order: 1. under simulated solar illumination, 2. in dark, 3. under simulated solar illumination. The first scan was omitted from the results.

2.5. Grazing incidence X-ray diffraction

The phase structure of the samples was investigated with Grazing Incidence X-ray diffraction (GIXRD, Panalytical X'Pert^3 PRO MRD) using Cu Kα radiation ($\lambda = 1.5405$ Å, $h\nu = 8.04$ keV) and 45 kV and 40 mA cathode voltage and current, respectively. The samples were scanned in 2θ between 22° and 52° by using a grazing-incidence angle of 0.3° for X-rays. The GIXRD measurements were conducted after the 3 + 27 nm TiO_2 ALD depositions and the tube furnace annealing. Thus the crystallinity of both the $TiSi_2$ film and the topmost TiO_2 film could be studied.

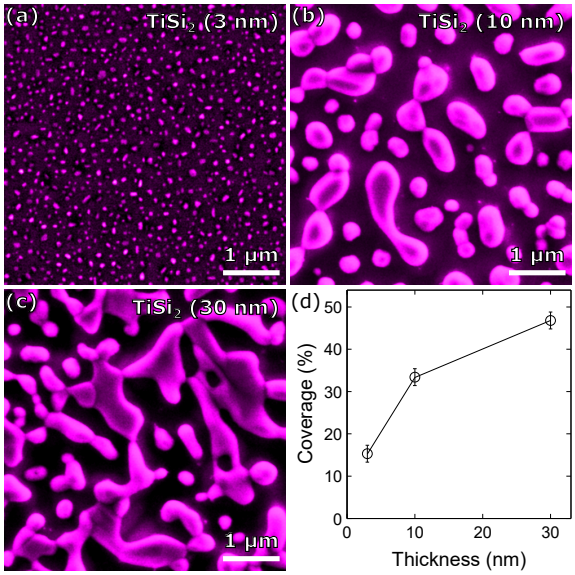

Figure 1: (a-c) Scanning electron microscopy (SEM) images of $TiSi_2$/Si surfaces. The thickness value (3, 10 or 30 nm) indicates the original TiO_2 layer thickness used for the silicide formation. (d) The $TiSi_2$ island coverage shows sublinear growth as a function of the TiO_2 layer thickness.

3. Results and discussion

3.1. Topographical and structural properties of the $TiSi_2$ islands

As shown in our previous study [28], a 30 nm thick ALD grown TiO_2 layer can be converted into highly topographically microstructured $TiSi_2$ patterns. In the present study, more attention is paid to controlling and understanding the structural and electronic properties of the $TiSi_2$ interlayer. Figure 1 shows the scanning electron microscope (SEM) images of three different $TiSi_2$ layers that are fabricated from the 3, 10, and 30 nm thick TiO_2 ALD films. As can be seen, the thickness strongly affects the structure of the $TiSi_2$ surface. In the case of a 3 nm film, the structure consists of clearly separated $TiSi_2$ islands with a diameter variation approximately from 10 to 100 nm. With a thicker 10 nm film the TiO_2 to $TiSi_2$ transformation leads to much bigger islands with a diameter range from approximately 50 nm to 500 nm. In addition, some coalescence

can be observed in this case but most of the islands are still detached from each other. Interesting change happens between the 10 nm and 30 nm layer thicknesses, where most of the $TiSi_2$ patterns start to coalesce into a continuous $TiSi_2$ network. As will be discussed later in more detail, this has a significant effect on the charge transfer properties. $TiSi_2$ has much lower resistivity than, for example, the underlying Si substrate. Thus a continuous $TiSi_2$ network enables the photogenerated charge carriers to escape along the surface plane instead of conducting them through the layer structure. Also the total coverage of the $TiSi_2$ patterns increases as the original TiO_2 film and island size become bigger. This is illustrated in Figure 1(d).

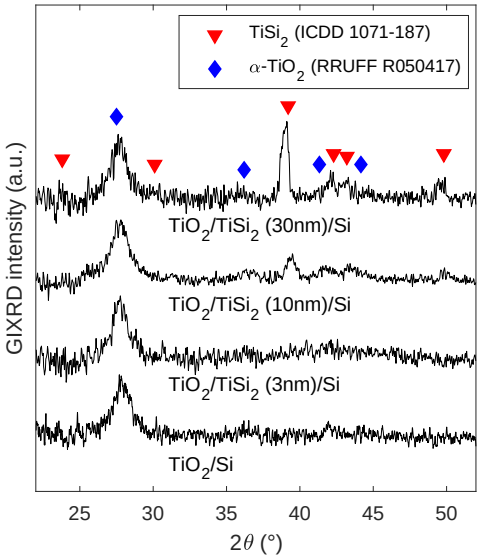

Figure 2: GIXRD patterns from $TiO_2/TiSi_2/Si(100)$ heterojunction systems. The diffraction patterns show that the original 3, 10 or 30 nm thick TiO_2 film has been converted into $TiSi_2$ during the UHV annealing. The topmost TiO_2 film has been crystallized into rutile (α-TiO_2) during the 400 °C annealing in air. The numbers in the legend correspond to XRD references in ICDD [37] and RRUFF [38] databases.

Figure 2 shows the GIXRD patterns measured from the $TiO_2/TiSi_2/Si(100)$ heterojunction systems without $TiSi_2$ and with 3, 10 and 30 nm $TiSi_2$ interlay-

ers. Only rutile (α-TiO_2) and $TiSi_2$ related diffraction maxima can be observed. The intensity of the rutile peaks remains similar on all four samples, which is expected because the TiO_2 film thickness is 30 nm on all four samples. On the other hand, the intensity of the $TiSi_2$ main peak at $2\theta = 39.2°$ shows some correlation with the thickness of the TiO_2 film that was used for $TiSi_2$ fabrication and also the $TiSi_2$ coverage.

3.2. Photoelectrochemical activity and charge transfer resistance

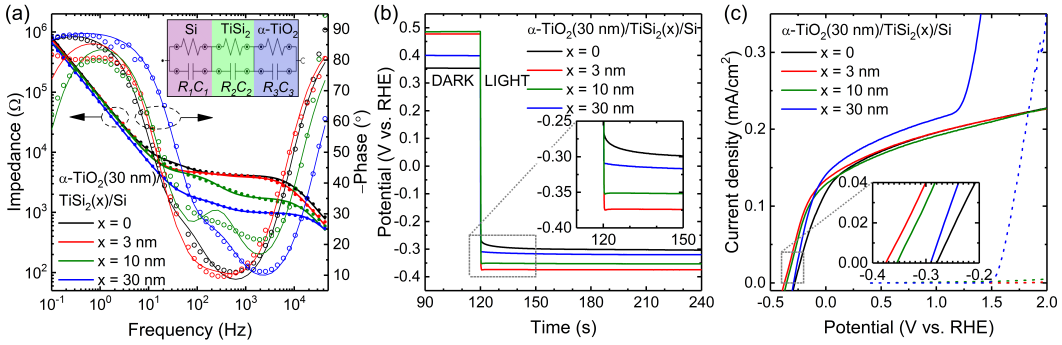

Figure 3: Photoelectrochemical analysis of α-TiO_2/$TiSi_2$/Si heterojunction systems in 1 M NaOH. (a) EIS Bode plots showing impedance (solid symbols) and phase shift (open symbols) measured at the OCP in dark before applying any bias potential. Electrochemical equivalent circuit used for EIS data modelling is shown as an inset in (a) and solid lines show the fits. (b) Chopped light OCP measurement. (c) Linear scan voltammetry measured at 50 mV/s in dark (dashed lines) and under simulated solar illumination (solid lines).

Figure 3 illustrates the results of the PEC analysis for all four α-TiO_2/$TiSi_2$/Si samples with varying $TiSi_2$ interlayer thicknesses. The EIS data in (a) reveals that the samples with a $TiSi_2$ interlayer show lower impedance compared to the sample without $TiSi_2$, in particular, in the medium frequency range (0.1–1 kHz). The simplified electric equivalent circuit (EEC) that adequately describes the measured EIS data in (a) has three parallel R and C elements in series, $(RC)(RC)(RC)$. The first (R_1C_1) describes the depletion zone of the Si substrate, the second (R_2C_2) the TiO_2/Si interface, and the third (R_3C_3) the TiO_2 layer capacitance. We note that the two time constant model $(RC)(RC)$ that is

typically applied to SiO_2/Si electrodes is not adequate to describe the samples with the interfacial $TiSi_2$, which gives rise to the additional time constant in the medium frequency range (0.1–1 kHz) [39]. The fitted EEC parameters are presented in Table 1. The TiO_2 layer capacitance (C_3) is directly proportional to the electrochemically active surface area. Therefore, the increased C_3 value of the sample with the 30 nm $TiSi_2$ interlayer stems from the more rough surface morphology in line with Ref. [28].

Table 1: Fitted EIS data for α-TiO_2/$TiSi_2$/Si heterojunction systems using $(RC)(RC)(RC)$ electric equivalent circuit.

TiO_2(30 nm)/$TiSi_2$(x)/Si	R_1 (kΩ)	C_1 (nF)	R_2 (kΩ)	C_2 (μF)	R_3 (MΩ)	C_3(μF)	χ^2
x = 0 nm	4.1	4.7	2.2	1.4	14.3	1.9	0.13
x = 3 nm	3.9	6.1	0.8	0.9	2.8	2.0	0.35
x = 10 nm	1.7	7.2	2.5	0.4	1.2	2.0	0.54
x = 30 nm	1.0	6.2	0.6	1.2	11.0	2.4	0.04

The chopped light OCP measurement in Figure 3(b) shows a negative shift in the OCP upon illumination for all four samples, which is characteristic to n-type photoelectrodes. However, the photoresponse is faster and the photovoltage is higher for the 3 and 10 nm $TiSi_2$ interlayers when compared to the samples without $TiSi_2$ or with the 30 nm coalesced $TiSi_2$ layer. Also, the photocurrent onset potentials were more negative than the ones we reported for similar ALD TiO_2 (30 nm)/Si photoanodes after different heat-treatment temperatures between 200 °C and 500 °C [36]. Therefore, it can be concluded that thin enough $TiSi_2$ interlayers improve the charge carrier separation at the TiO_2/Si interface and facilitate a more favorable band bending. Finally, the photocurrent onset potential for water oxidation in the Figure 3(c) shows a significant shift (70–100 mV) to more negative values for the 3 and 10 nm $TiSi_2$ interlayers when compared to the samples without $TiSi_2$ or with the 30 nm coalesced $TiSi_2$ layer. The improved charge separation and more negative onset potential are also supported by the SPV experiments made in UHV conditions. Under strong UV

illumination the samples with the 3 and 10 nm $TiSi_2$ interlayers exhibit highest surface photovoltage (See supplementary information Figure S1 for details.)

An interesting detail in the Figure 3(c) is the rapid increase in both dark and light currents around 1.5 V vs. RHE for the sample with the 30 nm $TiSi_2$ interlayer. Such an increase in the dark current, i.e. oxidation of H_2O without light, is an indication of low charge transfer resistance of the $TiSi_2$/Si substrate, which may be a consequence of the possible doping of n-Si with Ti [40] during the $TiSi_2$ synthesis at 950 °C. The slightly higher saturation photocurrent of the sample with the 30 nm $TiSi_2$ interlayer, on the other hand, is assigned to stronger TiO_2 absorption that is induced by more rough surface morphology as pointed out above.

3.3. Molecular bonding of the TiO_2/$TiSi_2$/Si heterojunction

Understanding how the $TiSi_2$ interlayer affects the charge transfer properties, the molecular bonding in addition to the band energy diagram of the TiO_2/$TiSi_2$/Si heterojunction needs to be determined. Therefore, the samples were studied in a stepwise manner with both XPS and UPS. Ti 2p, Si 2p, O 1s, VB and WF values (secondary electron cutoff features) were measured and analyzed at each step: on a clean Si surface, after formation of the $TiSi_2$ interlayers, and finally after deposition of the 3 nm TiO_2 layer on top of the $TiSi_2$ interlayers. Figure S2 illustrates the development of the Si 2p and Ti 2p core level spectra measured on a clean Si surface and the three different $TiSi_2$ layers. As can be seen, the 950 °C $TiSi_2$ formation temperature is adequate for removing practically all oxide components from both Si and Ti, i.e. there are no $2p_{3/2}$ photoelectron peaks at 103 or 459 eV binding energy regions corresponding to the Si and Ti oxides, respectively [41]. The Si 2p spectrum of the cleaned substrate consists only of the doublet separated elemental 1/2 and 3/2 states at $E_{b,(3/2)} = 99.25 \pm 0.05$. After the $TiSi_2$ formation, an additional doublet state appears at $E_{b,(3/2)} = 98.85 \pm 0.05$ eV corresponding to the Ti bound Si atoms. The area of this peak correlates well with the increasing $TiSi_2$ coverage observed in the SEM images. For Ti 2p, only one doublet state is detected at

$E_{b,(3/2)}$ = 458.68±0.05 eV originating from the silicidized Ti. Also in this case the area of the peak increases concurrently with the Si_{TiSi_2} peak area and the $TiSi_2$ island coverage. Figure S3 shows the valence band maxima (VBM) for the Si and $TiSi_2$/Si surfaces, and the corresponding WF values analyzed from the secondary electron cutoff are depicted in Figure S4. The VBM of $TiSi_2$ is located at the Fermi level within the experimental error. This is as expected, because $TiSi_2$ in known to be nearly metallic material with a low resistivity [42].

The WF values for both the clean Si and the three different $TiSi_2$/Si surfaces are close to each other. The 3 and 10 nm $TiSi_2$ layers exhibits a slightly higher WF value of 4.72 eV if compared to the WF value of clean Si (4.61 eV). However, the 30 nm $TiSi_2$ layer shows again almost the same average WF value as the clean Si. One noticeable difference is the increased dispersion in WF values in the case of the 30 nm $TiSi_2$ layer. The work function map shows a clear contrast between the $TiSi_2$ regions (highest WF) and the intervening Si areas (lowest WF). For the clean Si and the 3 and 10 nm $TiSi_2$ layers the work function maps are rather homogeneous. The difference between the TiSi surfaces can be explained by the "pinch-off" effect [43] where the barrier variation of sufficiently small island features becomes pinched off by the surrounding semiconductor regions. For example Rossi et al. [21, 22] have studied this phenomenon on electrolyte/Ni island/n-Si systems. With small Ni islands the effective barrier height drifts closer to that of the surrounding semiconductor surface. However, as the islands become larger, the band bending inside the islands behaves more independently and the barrier height moves closer to the barrier height of a continuous metallized surface. The size of the Ni islands studied by Rossi et al. varied from 20 nm to 1500 nm, and the upper limit of the island diameter for pinch-off was found to be approximately 350 nm. The result is in agreement with our measurements, where the 3 and 10 nm $TiSi_2$ layers with clearly sub-micrometer sized $TiSi_2$ features show almost no WF variation and the thickest 30 nm $TiSi_2$ has clearly distinct areas of different WF values. These large $TiSi_2$ islands prevent the pinch-off effect and lead to a lowered barrier height (lowered band bending), which decreases the charge separation performance. In the 3 and

10 nm layers the negative effect of the $TiSi_2$ particles on the barrier height gets pinched off, but the particles can still act as effective minority carrier collectors and thus promote the water splitting reaction [21].

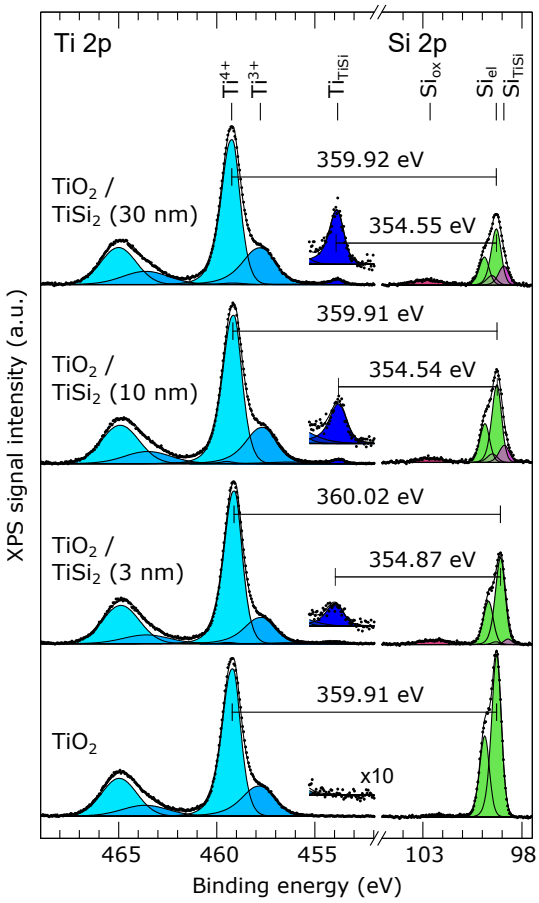

Figure 4: Ti 2p and Si 2p XP spectra of the $TiO_2/TiSi_2/Si$ heterojunctions. The spectral features originate from all three layers: the Si substrate, $TiSi_2$ interlayer (the bottom spectrum without $TiSi_2$, the upper spectra with $TiSi_2$ interlayers that were formed from the 3, 10, or 30 nm thick TiO_2 films) and the TiO_2 film (3 nm thick).

Figure 4 shows the Ti 2p and Si 2p XP spectra after the 3 nm TiO_2 deposition. The 3 nm film is thin enough so that all three layers (the Si substrate, $TiSi_2$ interlayer and TiO_2 film) can contribute their own chemical states to the spectra. The oxidized components of Ti (Ti^{4+} and Ti^{3+}) are similar for

each sample and represent a partially reduced ALD deposited TiO_2 film as reported in our previous studies [29, 36]. Also the previously mentioned Ti_{TiSi_2} can be detected through the TiO_2 film enabling the full band energy diagram reconstruction of the whole heterojunction. The Si 2p spectra resemble those measured in the previous step, just strongly attenuated due to the 3 nm TiO_2 overlayer. Additionally, a small amount of Si oxide is detected. The spatial distribution of SiO_x could not be resolved with the available resolution, but as we have previously shown [28], the $TiSi_2$ structures are resilient to oxidation. Thus the oxidation is assumed to happen on the Si areas that are not covered by the $TiSi_2$ islands.

3.4. Determination of the band energy diagram of the TiO_2/$TiSi_2$/Si heterojunction

In order to understand why the $TiSi_2$ interlayer affects the onset potential and charge transport properties of the three-layer photoanode system, a complete band energy diagram was reconstructed. Figure 5 shows the band positions of VBM, CBM, E_{vac} and selected core levels for each intermediate deposition step and all three different $TiSi_2$ film thicknesses. The band energy diagram of the cleaned Si substrate is shown in figure 5(a). The E_g value of 1.12 eV for Si bulk was taken from the literature [4] and the $(E_F - \mathrm{VBM})_{\mathrm{bulk}}$ distance of 0.85 eV was calculated from the silicon wafer resistivity [44]. The band gap for amorphous TiO_2 was determined by measuring the optical absorption of the film with a spectrophotometer. The details of this measurement are shown in the supplementary information (Figure S5).

The SPV corrected binding energy of the Si $2p_{surf}$ was evaluated from XPS measurements. Based on the silicon resistivity, the depletion width is several hundreds of nanometers [45]. Thus, it is valid to assume that the band positions within the XPS and UPS information depth are constant and reflect the band positions of the surface.

The distance between the Si 2p and Si VBM was evaluated from XPS and UPS measurements. The obtained value of 98.68 eV is in good agreement with

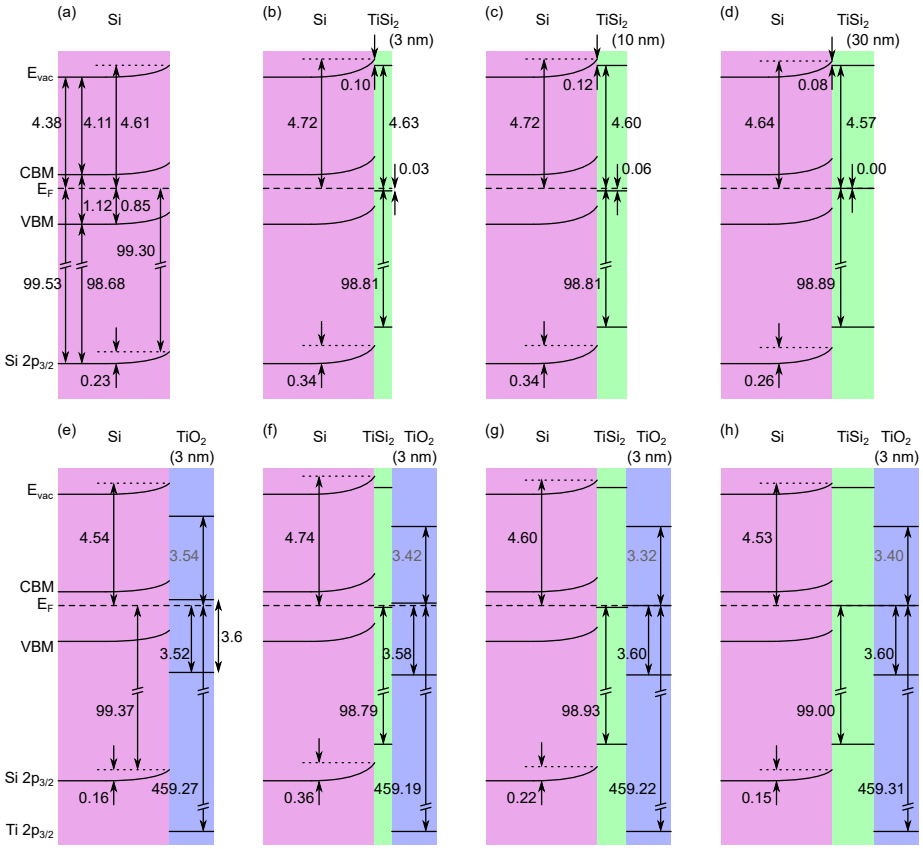

Figure 5: Band energy diagram of the clean Si (a), titanium silicide coated Si with different $TiSi_2$ interlayers (3, 10, and 30 nm) (b-d), and $TiO_2/TiSi_2/Si$ heterojunction systems where 3 nm of TiO_2 has been deposited on top of structure (e-h).

the value of 98.72 eV for the TiO_2/Si heterojunction by Hu et al. [4] The knowledge of the above-mentioned energies allowed the calculation of the 0.23 eV upward band bending for the cleaned Si surface. Combining this information with the WF value (4.61 eV) determined from the UPS secondary electron cutoff edge and the literature based E_g (1.12 eV) allowed us to calculate the CBM and E_{vac} positions above the E_F for both the surface and the bulk phases of Si. As a result of these calculations we obtained an electron affinity (χ) value of 4.11 eV for bulk Si. This is in reasonable agreement with the generally accepted value of 4.05 eV [46, 47] and the value of 4.07 eV obtained by Hu et al. [4]. This

result can thus be considered as a convenient validation of all the previously mentioned calculations and literature value based assumptions.

Figures 5(b)–(d) illustrate the similar band diagrams for $TiSi_2$/Si systems, where the $TiSi_2$ structure has been fabricated from the 3, 10, or 30 nm thick TiO_2 films. Most notably, the 3 and 10 nm $TiSi_2$ structures increase the band bending of the underlying Si substrate by about 0.1 eV leading to a total upward bending of 0.34 eV. Also the Si with the 30 nm $TiSi_2$ interface shows a 0.03 eV higher band bending than the clean Si substrate, but this small change is near the experimental detection limit. It should be noted, that the band positions represent the spatially averaged values at the surface. It is possible that the band bending is even stronger near the $TiSi_2$ islands but the small size of the islands prevents the spatially resolved mapping of the localized band energies.

Based on the E_{vac} values of the Si and $TiSi_2$, there is a 0.1 eV surface dipole (δ) at the $TiSi_2$/Si interface with the redistribution of electron density towards the Si substrate. This dipole at least partially accounts for the increased Si band bending when the $TiSi_2$ structure is fabricated on the surface [4, 33].

Figures 5(e)–(h) represent the band diagrams for TiO_2/Si and TiO_2/$TiSi_2$/Si interfaces, where the $TiSi_2$ interfaces, the thickness of which range from 3 to 30 nm, are covered by the 3 nm TiO_2 overlayer. Also in this case the strongest Si band bending is observed for the junctions where the $TiSi_2$ structure has been fabricated from the 3 and 10 nm TiO_2 films. On the other hand, the TiO_2/Si system without a $TiSi_2$ interlayer and also the TiO_2/$TiSi_2$/Si with the 30 nm $TiSi_2$ interlayer express a weaker band bending. Given that the $TiSi_2$ induced band bending of Si is only little affected by the TiO_2 overlayer, it is reasonable to assume that the band bending is similar under the amorphous TiO_2 that was used in the PES measurements and the rutile TiO_2 that was used in the PEC test.

The possibility of adjusting the band bending by altering the $TiSi_2$ layer thickness and coverage provides a powerful way to tune the VBM and CBM offsets. This on the other hand affects the charge separation and charge transport properties across the heterojunction. The band offset between the Si and

TiO_2 can be calculated based on the Kraut's method [48, 49] using the following equation

$$\begin{aligned}&\Delta E_{\mathrm{VBM}}\\&= (E_{\mathrm{Ti\ 2p}} - E_{\mathrm{Si\ 2p}})_{\mathrm{TiO_2/Si}} - [(E_{\mathrm{Ti\ 2p}} - E_{\mathrm{VBM}})_{\mathrm{TiO_2}} - (E_{\mathrm{Si\ 2p}} - E_{\mathrm{VBM}})_{\mathrm{Si}}]\,,\end{aligned} \tag{1}$$

where the subscripts inside the parentheses denote the specific energy levels and the subscripts outside the parentheses denote the material systems, i.e. TiO_2/Si heterojunction or Si and TiO_2 bulk references. In our case the Si and TiO_2 VBMs are located far from each other and the underlying Si substrate gives only a very weak signal in the extremely surface sensitive UPS measurement. Thus, the TiO_2 VBM position can be determined more accurately by measuring it directly from the studied heterojunction samples instead of a bulk reference sample. For this reason the equation can be simplified to

$$\Delta E_{\mathrm{VBM}} = (E_{\mathrm{VBM}})_{\mathrm{TiO_2}} - (E_{\mathrm{Si\ 2p}})_{\mathrm{TiO_2/Si}} - (E_{\mathrm{Si\ 2p}} - E_{\mathrm{VBM}})_{\mathrm{Si}}. \tag{2}$$

Knowing the band gap for both Si and TiO_2 also enables the calculation of the CBM offsets when the VBM offsets are known. Figure 6 illustrates these offsets for the heterojunction samples with the 3, 10, and 30 nm $TiSi_2$ interlayers. Smallest offsets are observed when the TiO_2 film is deposited directly to the clean Si surface and also in the case of the 30 nm $TiSi_2$ interlayer. On the other hand, the 3 and 10 nm $TiSi_2$ layers increase the band offsets thus leading to a higher photovoltage, which improves the separation of excited charge carriers. VBM offsets ranging from 1 eV up to 2.73 eV have been reported by for TiO_2/Si heterojunctions [50, 51, 52, 12]. The large variation shows that the VBM offset is sensitive to both the preparation method of the TiO_2 film and the interlayer between the Si substrate and the TiO_2 film. For example Perego et al. [12] have reported an offset variation of 0.3 eV by changing the composition of an approximately 2 nm thick interlayer between the Si and TiO_2 layers. The magnitude of the variation is well in line with our observations, although in our case only the topographical properties instead of the composition are varied.

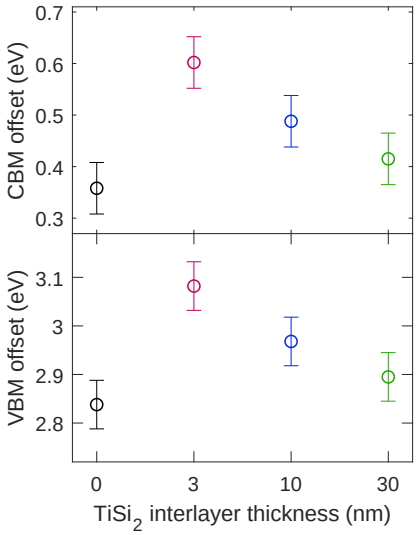

Figure 6: Valence band maximum (VBM) and conduction band minimum (CBM) offsets for $TiO_2/TiSi_2/Si$ heterojunction systems with 0, 3, 10, and 30 nm $TiSi_2$ interlayer thicknesses.

Despite the improved photovoltage and charge carrier separation, higher band offset also means larger barrier height against charge transport across the junction. This means that the hole injection from the Si side to the TiO_2 side along the VB or the electron injection from the TiO_2 side to the Si side along the CB becomes more obstructed. At first this may seem contradictory to the PEC results, where the 3 and 10 nm $TiSi_2$ interlayers resulted in smaller onset potential and larger or equal photocurrent than without the $TiSi_2$ interlayer or with the 30 nm $TiSi_2$ interlayer.

The above mentioned results can be rationalized based on a Z-scheme model [23, 24, 25]. In this model the non-interconnected metal-like $TiSi_2$ islands endow recombination centers inside the heterojunction. As schematically illustrated in Figure 7, the $TiSi_2$ islands improve the charge separation by increasing the Si band bending and also provide a low resistance charge transfer channel through the native SiO_2. Electrons from the TiO_2 overlayer recombine with the holes from the Si substrate inside the metallic $TiSi_2$ islands according to the Z-scheme mechanism for overall charge transport.

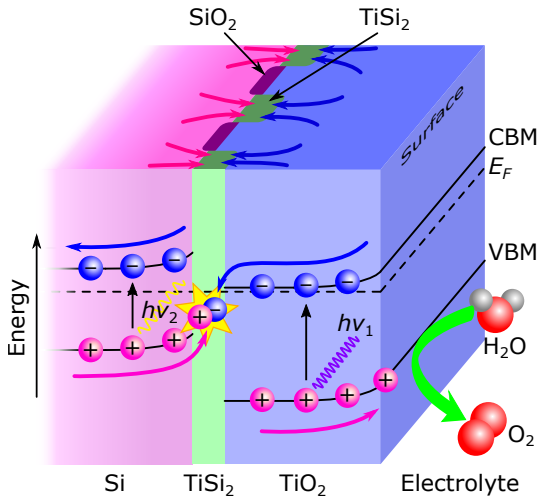

Figure 7: Schematic illustration of the charge transfer channels in a Z-scheme $TiO_2/TiSi_2/Si$ three-layer photoanode in PEC conditions.

Photons that have higher energy than the TiO_2 band gap can be absorbed in the TiO_2 film and thus produce photogenerated electron–hole pairs. Similarly lower energy photons excite electrons in the underlying Si substrate. In the Z-scheme model the net charge transfer leads to the accumulation of holes on the outer surface of the TiO_2 film and electron accumulation in the Si bulk. In PEC conditions the surface accumulated holes are then readily available for water oxidation.

4. Conclusions

The results constitute a comprehensive study of the electronic structure of $TiO_2/TiSi_2/Si$ systems that can be utilized as photoanodes in water splitting reaction. ALD grown "leaky" TiO_2 has been found to exhibit protective and photoactive properties, and it can be used as a buffer layer between the electrolyte and small band gap semiconductors. In this study we used micropatterned $TiSi_2$ interlayer for tailoring the electronic properties of the TiO_2/Si interface. XPS and UPS measurements show that the modification of the $TiSi_2$ interlayer has direct effect on the band alignment across the heterojunction. $TiSi_2$ layers that

are thermally formed from the 3 and 10 nm thick TiO_2 films lead to the strongest band bending and largest band offsets. The $TiSi_2$ islands in these structures are small enough for the pinch-off effect, whereas the $TiSi_2$ interlayer formed from the 30 nm TiO_2 film leads to large coalesced $TiSi_2$ islands where the pinch-off effect does not affect any more. This lowers the band bending and decreases the photovoltaic efficiency by reducing the charge carrier separation and shifting the onset potential to more positive values. Based on the photoelectrochemical measurements, the samples with the highest band offset ($TiSi_2$ from the 3 and 10 nm films) yield the best water splitting performance despite their increased barrier height for minority carriers migrating across the junction. This can be explained by the Z-scheme model, where the $TiSi_2$ islands at the heterojunction interface act as recombination centers providing an energetically favorable route for overall charge transport.

5. Acknowledgement

This work was supported by the Academy of Finland [grant numbers 141481, 286713 and 309920]. M. H. was supported by the TUT's Graduate School and Emil Aaltonen foundation. H. A. was supported by the Jenny and Antti Wihuri Foundation. We thank R. Ulkuniemi for operating the spectrophotometer during the UV-Vis absorption measurements.

References

References

[1] A. Fujishima, K. Honda, Electrochemical photolysis of water at a semiconductor electrode, Nat. 238 (1972) 37. doi:10.1038/238037a0.
URL http://dx.doi.org/10.1038/238037a0

[2] M. G. Walter, E. L. Warren, J. R. McKone, S. W. Boettcher, Q. Mi, E. A. Santori, N. S. Lewis, Solar water splitting cells, Chem. Rev. 110 (11) (2010) 6446–6473.

[3] Y. W. Chen, J. D. Prange, S. Dühnen, Y. Park, M. Gunji, C. E. D. Chidsey, P. C. McIntyre, Atomic layer-deposited tunnel oxide stabilizes silicon photoanodes for water oxidation, Nat. Mater. 10 (2011) 539–544.

[4] S. Hu, M. H. Richter, M. F. Lichterman, J. Beardslee, T. Mayer, B. S. Brunschwig, N. S. Lewis, Electrical, photoelectrochemical, and photoelectron spectroscopic investigation of the interfacial transport and energetics of amorphous TiO_2/Si heterojunctions, The J. of Phys. Chem. C 120 (6) (2016) 3117–3129. doi:10.1021/acs.jpcc.5b09121.
URL https://doi.org/10.1021/acs.jpcc.5b09121

[5] B. Seger, D. S. Tilley, T. Pedersen, P. C. K. Vesborg, O. Hansen, M. Gratzel, I. Chorkendorff, Silicon protected with atomic layer deposited TiO_2: durability studies of photocathodic H_2 evolution, RSC Adv. 3 (2013) 25902–25907. doi:10.1039/C3RA45966G.
URL http://dx.doi.org/10.1039/C3RA45966G

[6] K. Sivula, Defects give new life to an old material: Electronically leaky titania as a photoanode protection layer, ChemCatChem 6 (10) (2014) 2796–2797.
URL http://dx.doi.org/10.1002/cctc.201402532

[7] J. Gu, Y. D. Yan, J. L. Young, K. X. Steirer, N. R. Neale, J. A. Turner, Water reduction by a p-$GaInP_2$ photoelectrode stabilized by an amorphous TiO_2 coating and a molecular cobalt catalyst, Nat. Mater. 15 (2016) 456–460. doi:10.1038/nmat4511.

[8] J. Klett, J. Ziegler, A. Radetinac, B. Kaiser, R. Schäfer, W. Jaegermann, F. Urbain, J.-P. Becker, V. Smirnov, F. Finger, Band engineering for efficient catalyst-substrate coupling for photoelectrochemical water splitting, Phys. Chem. Chem. Phys. 18 (2016) 10751–10757. doi:10.1039/C5CP06230F.

[9] B. Seger, T. Pedersen, A. B. Laursen, P. C. K. Vesborg, O. Hansen,

I. Chorkendorff, Using TiO_2 as a conductive protective layer for photocathodic H_2 evolution, J. of the Am. Chem. Soc. 135 (3) (2013) 1057–1064, pMID: 23289745. arXiv:https://doi.org/10.1021/ja309523t, doi:10.1021/ja309523t.

[10] J. Yang, K. Walczak, E. Anzenberg, F. M. Toma, G. Yuan, J. Beeman, A. Schwartzberg, Y. Lin, M. Hettick, A. Javey, J. W. Ager, J. Yano, H. Frei, I. D. Sharp, Efficient and sustained photoelectrochemical water oxidation by cobalt oxide/silicon photoanodes with nanotextured interfaces, J. of the Am. Chem. Soc. 136 (17) (2014) 6191–6194, pMID: 24720554. arXiv:https://doi.org/10.1021/ja501513t, doi:10.1021/ja501513t.
URL https://doi.org/10.1021/ja501513t

[11] M. F. Lichterman, S. Hu, M. H. Richter, E. J. Crumlin, S. Axnanda, M. Favaro, W. Drisdell, Z. Hussain, T. Mayer, B. S. Brunschwig, N. S. Lewis, Z. Liu, H.-J. Lewerenz, Direct observation of the energetics at a semiconductor/liquid junction by operando X-ray photoelectron spectroscopy, Energy & Environ. Sci. 8 (2015) 2409–2416.
URL http://dx.doi.org/10.1039/C5EE01014D

[12] M. Perego, G. Seguini, G. Scarel, M. Fanciulli, F. Wallrapp, Energy band alignment at TiO_2/Si interface with various interlayers, J. of Appl. Phys. 103 (4) (2008) 043509. arXiv:https://doi.org/10.1063/1.2885109, doi:10.1063/1.2885109.
URL https://doi.org/10.1063/1.2885109

[13] P. E. Schmid, P. S. Ho, T. Y. Tan, Summary abstract: Correlation between schottky barrier height and phase stoichiometry/structure of silicide–silicon interfaces, J. of Vac. Sci. and Technol. 20 (3) (1982) 688–689. doi:10.1116/1.571629.

[14] J. Freeouf, Silicide schottky barriers: An elemental description, Solid State Commun. 33 (10) (1980) 1059–1061. doi:https://doi.org/10.1016/0038-1098(80)90317-8.

[15] J. M. Andrews, J. C. Phillips, Chemical bonding and structure of metal-semiconductor interfaces, Phys. Rev. Lett. 35 (1975) 56–59. doi:10.1103/PhysRevLett.35.56.

[16] J. L. Freeouf, Silicide interface stoichiometry, J. of Vac. Sci. and Technol. 18 (3) (1981) 910–916. doi:10.1116/1.570993.
URL https://doi.org/10.1116/1.570993

[17] M. A. Taubenblatt, C. R. Helms, Silicide and schottky barrier formation in the Ti–Si and the Ti–SiO_x–Si systems, J. of Appl. Phys. 53 (9) (1982) 6308–6315. doi:10.1063/1.331551.
URL https://doi.org/10.1063/1.331551

[18] R. T. Tung, J. M. Gibson, Single crystal silicide silicon interfaces: Structures and barrier heights, J. of Vac. Sci. & Technol. A 3 (3) (1985) 987–991. doi:10.1116/1.573372.

[19] R. T. Tung, Electron transport of inhomogeneous Schottky barriers, Appl. Phys. Lett. 58 (24) (1991) 2821–2823. doi:10.1063/1.104747.
URL https://doi.org/10.1063/1.104747

[20] R. T. Tung, Electron transport at metal-semiconductor interfaces: General theory, Phys. Rev. B 45 (1992) 13509–13523. doi:10.1103/PhysRevB.45.13509.
URL https://link.aps.org/doi/10.1103/PhysRevB.45.13509

[21] R. C. Rossi, M. X. Tan, N. S. Lewis, Size-dependent electrical behavior of spatially inhomogeneous barrier height regions on silicon, Appl. Phys. Lett. 77 (17) (2000) 2698–2700. doi:10.1063/1.1319534.

[22] R. C. Rossi, N. S. Lewis, Investigation of the Size-Scaling Behavior of Spatially Nonuniform Barrier Height Contacts to Semiconductor Surfaces Using Ordered Nanometer-Scale Nickel Arrays on Silicon Electrodes, J. Phys. Chem. B 105 (49) (2001) 12303–12318. doi:10.1021/jp011861c.
URL https://doi.org/10.1021/jp011861c

[23] S. Li, Q. Zhao, D. Wang, T. Xie, Work function engineering derived all-solid-state Z-scheme semiconductor-metal-semiconductor system towards high-efficiency photocatalytic H_2 evolution, RSC Adv. 6 (2016) 66783–66787. doi:10.1039/C6RA14680E.

[24] J.-M. Li, H.-Y. Cheng, Y.-H. Chiu, Y.-J. Hsu, ZnO-Au-SnO_2 Z-scheme photoanodes for remarkable photoelectrochemical water splitting, Nanoscale 8 (2016) 15720–15729. doi:10.1039/C6NR05605A.

[25] H. Tada, T. Mitsui, T. Kiyonaga, T. Akita, K. Tanaka, All-solid-state Z-scheme in CdS–Au–TiO_2 three-component nanojunction system, Nat. Mater. 5 (2006/09/10) 782. doi:10.1038/nmat1734.

[26] A. Zhang, G. Zheng, C. Lieber, Nanowires: Building Blocks for Nanoscience and Nanotechnology, 1st Edition, Springer International Publishing, 2016.

[27] C. Liu, Y. J. Hwang, H. E. Jeong, P. Yang, Light-induced charge transport within a single asymmetric nanowire, Nano Lett. 11 (9) (2011) 3755–3758. doi:10.1021/nl201798e.
URL https://doi.org/10.1021/nl201798e

[28] M. Hannula, K. Lahtonen, H. Ali-Löytty, A. Zakharov, T. Isotalo, J. Saari, M. Valden, Fabrication of topographically microstructured titanium silicide interface for advanced photonic applications, Scr. Mater. 119 (2016) 76–81.
URL http://dx.doi.org/10.1016/j.scriptamat.2016.03.016

[29] M. Hannula, H. Ali-Löytty, K. Lahtonen, E. Sarlin, J. Saari, M. Valden, Improved stability of atomic layer deposited amorphous TiO_2 photoelectrode coatings by thermally induced oxygen defects, Chem. of Mater. 30 (4) (2018) 1199–1208. doi:10.1021/acs.chemmater.7b02938.
URL https://doi.org/10.1021/acs.chemmater.7b02938

[30] C. Jin, B. Liu, Z. Lei, J. Sun, Structure and photoluminescence of the TiO_2 films grown by atomic layer deposition using tetrakis-dimethylamino titanium and ozone, Nanoscale Res. Lett. 10 (1) (2015) 95.

[31] J. Aarik, A. Aidla, A.-A. Kiisler, T. Uustare, V. Sammelselg, Effect of crystal structure on optical properties of TiO_2 films grown by atomic layer deposition, Thin Solid Films 305 (1) (1997) 270–273.
URL http://dx.doi.org/10.1016/S0040-6090(97)00135-1

[32] Omicron Nanotechnology, NanoESCA (2017).
URL http://www.scientaomicron.com

[33] D. C. Gleason-Rohrer, B. S. Brunschwig, N. S. Lewis, Measurement of the band bending and surface dipole at chemically functionalized Si(111)/vacuum interfaces, The J. of Phys. Chem. C 117 (35) (2013) 18031–18042.
URL https://doi.org/10.1021/jp401585s

[34] CasaXPS: Processing Software for XPS, AES, SIMS and More (2017).
URL http://www.casaxps.com

[35] O. Renault, R. Brochier, P.-H. Haumesser, N. Barrett, B. Krömker, D. Funnemann, Energy-filtered peem imaging of polycrystalline Cu surfaces with work function contrast and high lateral resolution, E-j. of Surf. Sci. and Nanotechnol. 4 (2006) 431–434.

[36] H. Ali-Löytty, M. Hannula, J. Saari, L. Palmolahti, B. D. Bhuskute, R. Ulkuniemi, T. Nyyssönen, K. Lahtonen, M. Valden, Diversity of TiO_2: Controlling the molecular and electronic structure of atomic-layer-deposited black TiO_2, ACS Appl. Mater. & Interfaces 11 (3) (2019) 2758–2762. doi:10.1021/acsami.8b20608.
URL https://doi.org/10.1021/acsami.8b20608

[37] ICDD, International Centre for Diffraction Data. (2018).

[38] RRUFF, integrated database of Raman spectra, X-ray diffraction and chemistry data for minerals. (2018).

[39] V. Bertagna, R. Erre, F. Rouelle, M. Chemla, S. Petitdidier, D. Levy, Electrochemical study for the characterisation of wet sil-

icon oxide surfaces, Electrochimica Acta 47 (1) (2001) 129–136. doi:https://doi.org/10.1016/S0013-4686(01)00569-2.
URL http://www.sciencedirect.com/science/article/pii/S0013468601005692

[40] T. Zhou, Y. Zuo, L. Li, K. Qiu, J. Zheng, Q. Wang, Structural, optical and electrical properties of Ti doped amorphous silicon prepared by co-sputtering, Vac. 104 (2014) 65–69. doi:https://doi.org/10.1016/j.vacuum.2014.01.004.

[41] NIST X-ray photoelectron spectroscopy database, NIST standard reference database number 20, National Institute of Standards and Technology, Gaithersburg MD, 20899 (2000). (2018). doi:10.18434/T4T88K.

[42] S. P. Murarka, D. B. Fraser, A. K. Sinha, H. J. Levinstein, Refractory silicides of titanium and tantalum for low-resistivity gates and interconnects, IEEE J. of Solid-State Circuits 15 (4) (1980) 474–482. doi:10.1109/JSSC.1980.1051425.

[43] J. L. Freeouf, T. N. Jackson, S. E. Laux, J. M. Woodall, Effective barrier heights of mixed phase contacts: Size effects, Appl. Phys. Lett. 40 (7) (1982) 634–636. doi:10.1063/1.93171.
URL https://aip.scitation.org/doi/abs/10.1063/1.93171

[44] W. R. Thurber, R. L. Mattis, Y. M. Liu, J. J. Filliben, Resistivity–dopant density relationship for phosphorus-doped silicon, J. of The Electrochem. Soc. 127 (1980) 1807–1812. doi:10.1149/1.2130006.

[45] H. Lüth, Solid Surfaces, Interfaces and Thin Films, 6th Edition, Springer, 2014.

[46] S. M. Sze, K. K. Ng, Physics of semiconductor devices, John Wiley & Sons, 2006.

[47] R. Hunger, R. Fritsche, B. Jaeckel, W. Jaegermann, L. J. Webb, N. S. Lewis, Chemical and electronic characterization of methyl-terminated

Si(111) surfaces by high-resolution synchrotron photoelectron spectroscopy, Phys. Rev. B 72 (2005) 045317. doi:10.1103/PhysRevB.72.045317.

[48] E. A. Kraut, R. W. Grant, J. R. Waldrop, S. P. Kowalczyk, Precise determination of the valence-band edge in X-Ray photoemission spectra: Application to measurement of semiconductor interface potentials, Phys. Rev. Lett. 44 (1980) 1620–1623. doi:10.1103/PhysRevLett.44.1620.
URL https://link.aps.org/doi/10.1103/PhysRevLett.44.1620

[49] E. A. Kraut, R. W. Grant, J. R. Waldrop, S. P. Kowalczyk, Semiconductor core-level to valence-band maximum binding-energy differences: Precise determination by X-ray photoelectron spectroscopy, Phys. Rev. B 28 (1983) 1965–1977. doi:10.1103/PhysRevB.28.1965.
URL https://link.aps.org/doi/10.1103/PhysRevB.28.1965

[50] C. C. Fulton, G. Lucovsky, R. J. Nemanich, Electronic states at the interface of Ti—Si oxide on Si(100), J. of Vac. Science & Technol. B: Microelectron. and Nanom. Struct. Process., Meas., and Phenom. 20 (4) (2002) 1726–1731. arXiv:https://avs.scitation.org/doi/pdf/10.1116/1.1493785, doi:10.1116/1.1493785.
URL https://avs.scitation.org/doi/abs/10.1116/1.1493785

[51] C. C. Fulton, G. Lucovsky, R. J. Nemanich, Process-dependent band structure changes of transition-metal (Ti,Zr,Hf) oxides on Si(100), Appl. Phys. Lett. 84 (4) (2004) 580–582. arXiv:https://doi.org/10.1063/1.1639944, doi:10.1063/1.1639944.
URL https://doi.org/10.1063/1.1639944

[52] S. A. Campbell, D. C. Gilmer, X.-C. Wang, M.-T. Hsieh, H.-S. Kim, W. L. Gladfelter, J. Yan, MOSFET transistors fabricated with high permitivity TiO_2 dielectrics, IEEE Trans. on Electron Devices 44 (1) (1997) 104–109. doi:10.1109/16.554800.

Supplementary material

Highly efficient charge separation in Z-scheme $TiO_2/TiSi_2/Si$ photoanode by micropatterned titanium silicide interlayer

M. Hannula[a], H. Ali-Löytty[a], K. Lahtonen[a], J. Saari[a], A. Tukiainen[b], M. Valden[a,*]

[a]Surface Science Group, Laboratory of Photonics, Tampere University of Technology, P.O. Box 692, FI-33101 Tampere, Finland [b]Optoelectronics Research Centre, Laboratory of Photonics, Tampere University of Technology, P.O. Box 692, FI-33101 Tampere, Finland

*Corresponding author:
Email address: mika.valden@tut.fi
URL: www.tut.fi/surfsci

UV induced SPV of the $TiO_2/TiSi_2/Si$ surfaces

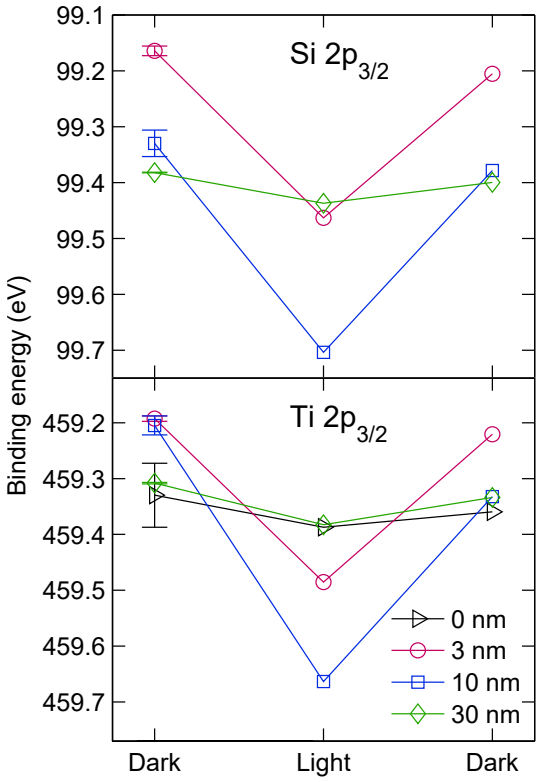

Figure S1: Position of the Si 2p and Ti 2p core levels with and without UV light. The samples with the 3 and 10 nm $TiSi_2$ interlayer show strong reversible band flattening due to UV induced surface photovoltage.

As described in the main article, the X-ray induced SPV effect was eliminated or at least mitigated by using a lower X-ray power when noticeable band flattening was detected. However, to test the optical response of the TiO_2 (3nm)/$TiSi_2$/Si systems, Ti 2p and Si 2p core levels were measured also under strong UV illumination. The UV light was produced with an Osram HBO 103W/2 short arc Hg lamp (main peak at 238 eV, cutoff filter at 260 nm for removing visible and IR radiation) that, unlike the focused X-ray source, illuminated a large area of the sample surface. Figure S1 illustrates the position of the Si 2p and Ti 2p core levels in dark (only X-ray illumination) and in light (X-ray and UV light). The SPV shows clear correlation with the PEC onset potential. The 3 and 10 nm $TiSi_2$ interlayers that had the lowest onset potential, also show strongest band flattening. On the other hand, for TiO_2/Si without $TiSi_2$ and also $TiO_2/TiSi_2$/Si system with the 30 nm interlayer, the SPV is almost negligible. For the 30 nm layer this can be associated with the coalescence of the $TiSi_2$ islands, which effectively leads to a continuous metallization layer between the Si substrate and the TiO_2 film. The result is similar to that of Waddill et al. [1] when they observed that forming a connection between Ni dots in a Ni/GaAs

system leads to the formation of a conduction path from the illuminated region to the edges of the sample, where the ohmic contact is stronger. This allows compensation of the SPV and prevents the UV light induced band flattening, because the minority carriers cannot accumulate to the surface. On the other hand, the $TiSi_2$ islands formed from the 3 and 10 nm TiO_2 films are not connected to each other and cannot conduct current along the surface. Thus, they serve only as charge transfer channels across the heterojunction and do not provide compensation for the SPV.

Ti 2p and Si 2p XP spectra of the $TiSi_2$/Si surfaces

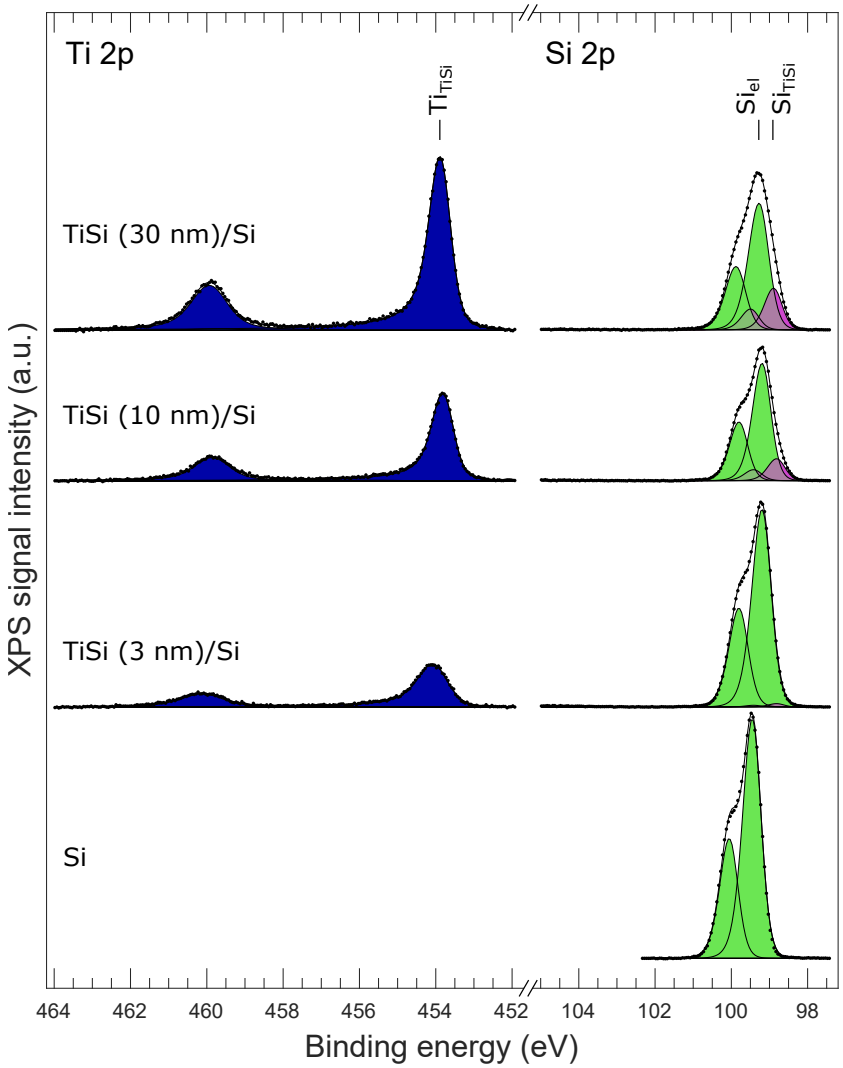

Figure S2: Ti 2p and Si 2p XP spectra of the $TiSi_2$/Si surfaces before applying the topmost TiO_2 film. The spectral features originate from both the Si substrate and the $TiSi_2$ interlayer. The bottom spectrum shows the cleaned Si without $TiSi_2$, and the upper spectra are from samples with $TiSi_2$ layers, that were formed from 3, 10, or 30 nm thick TiO_2 films).

Valence band maximum of the $TiSi_2$/Si surfaces

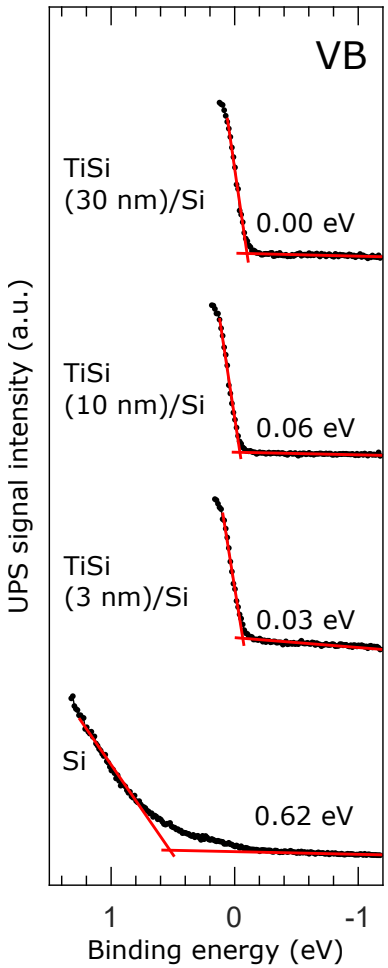

Figure S3: Valence band maximum (VBM) of the Si and $TiSi_2$/Si surfaces. The bottom spectrum shows the cleaned Si without $TiSi_2$, and the upper spectra are from samples with $TiSi_2$ layers, that were formed from 3, 10, or 30 nm thick TiO_2 films).

Localized work function of the $TiSi_2$/Si surfaces

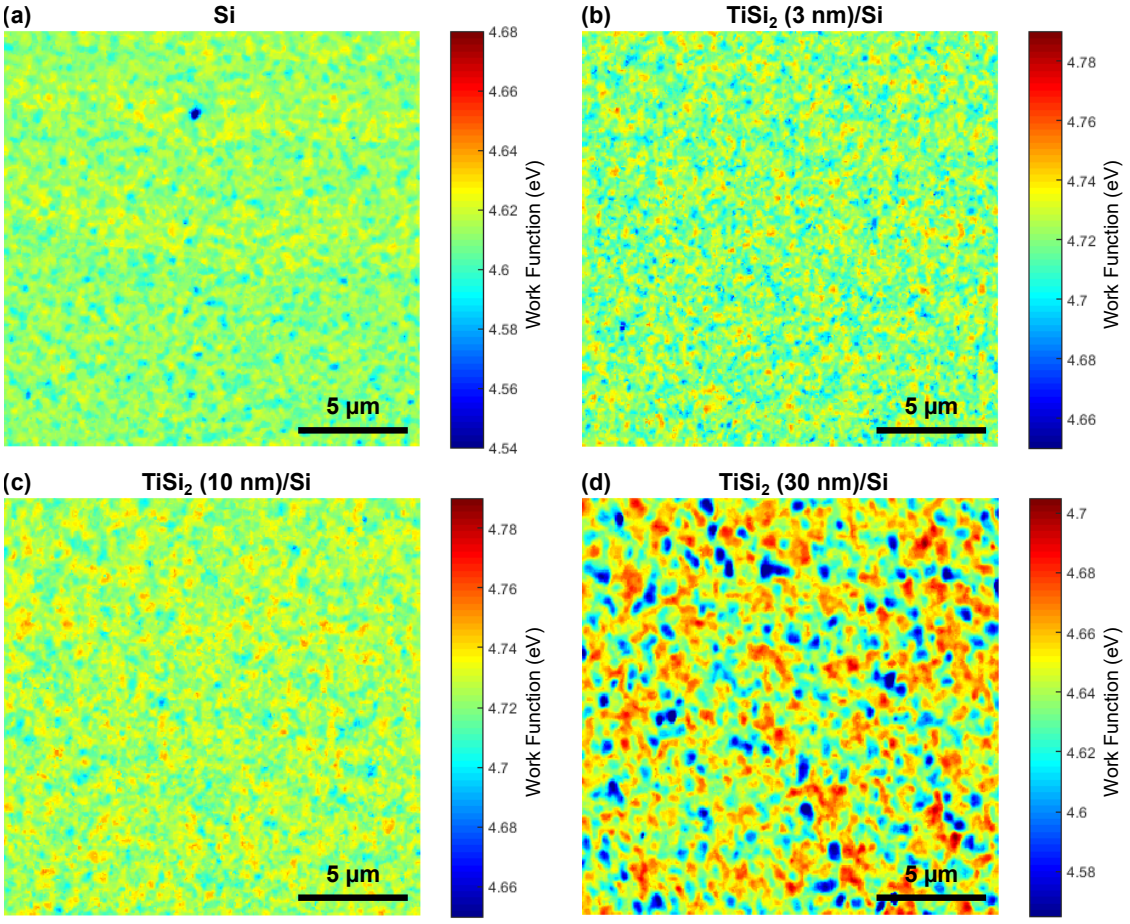

Figure S4: Work function (WF) of the Si and $TiSi_2$/Si surfaces. (a) shows the cleaned Si without $TiSi_2$, and (b)–(d) are from samples with $TiSi_2$ layers, that were formed from 3, 10, or 30 nm thick TiO_2 films). The work function values are determined as the intersection between the linear portion of the secondary electron cut-off edge and the background level on the low kinetic energy side from the edge. The fitting was made individually for each pixel in the image stack measured as a function of energy.

Determination of the optical band gap of amorphous TiO_2

The optical band gap (E_g) of the TiO_2 was determined by measuring the optical absorption of the film. The optical properties were measured on 30 and 200 nm thick TiO_2 films deposited on fused quartz (FQ) substrates. With two different film thicknesses, we were able to verify that the thickness does not affect the calculated E_g value. Measurements were conducted by measuring both the transmission and reflectance of the TiO_2 film with an integrating sphere detector. Due to the relatively high reflectance, a reflection corrected formula was used for calculating the absorption coefficient:

$$\alpha = -\frac{1}{x} \ln \frac{T}{1-R}, \tag{1}$$

where x is the thickness of the TiO_2 film, T is the transmission and R is the reflectance.

For the determination of the E_g, a curve of $(\alpha \times h\nu)^n$ vs. $h\nu$ can be drawn. Here h is the Planck constant, ν the frequency of the incoming radiation and n depends on the type of the E_g. For TiO_2 the band gap is indirect, which corresponds to $n = 1/2$. The intersection of the linear parts of the curve is equal to the value of the E_g.

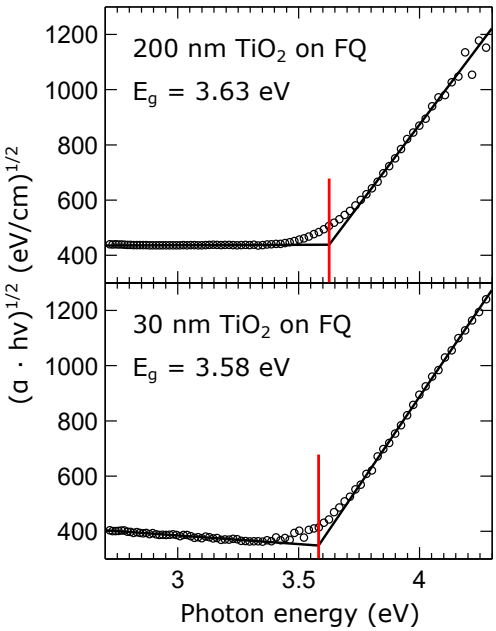

Figure S5: The reflection corrected optical absorption data of 30 and 200 nm thick TiO_2 films on fused quartz (FQ) substrate. Both film thicknesses reveal an indirect band gap of 3.60 ± 0.03 eV.

Figure S5 illustrates the results calculated with the Equation (1). Both 30 and 200 nm film thicknesses revealed an optical band gap of 3.60 ± 0.03 eV, where the variation is well within the experimental error. Also, the obtained band gap is in line with the literature, where values ranging from 3.4 to 3.64 eV have been reported for amorphous TiO_2 [2, 3, 4].

References

[1] G. D. Waddill, T. Komeda, Y.-N. Yang, J. H. Weaver, Photoemission from metal dots on GaAs(110): Surface photovoltages and conductivity, Phys. Rev. B 41 (1990) 10283–10286. doi:10.1103/PhysRevB.41.10283.
URL https://link.aps.org/doi/10.1103/PhysRevB.41.10283

[2] S. Valencia, J. Marín, G. Restrepo, Study of the bandgap of synthesized titanium dioxide nanoparticules using the sol-gel method and a hydrothermal treatment, The Open Materials Science Journal 4 (2010) 9–14. doi:10.2174/1874088X01004020009.

[3] Y. Gao, Y. Masuda, Z. Peng, T. Yonezawa, K. Koumoto, Room temperature deposition of a TiO_2 thin film from aqueous peroxotitanate solution, J. Mater. Chem. 13 (2003) 608–613. doi:10.1039/B208681F.
URL http://dx.doi.org/10.1039/B208681F

[4] T. Asanuma, T. Matsutani, C. Liu, T. Mihara, M. Kiuchi, Structural and optical properties of titanium dioxide films deposited by reactive magnetron sputtering in pure oxygen plasma, Journal of Applied Physics 95 (11) (2004) 6011–6016. doi:10.1063/1.1728313.
URL https://doi.org/10.1063/1.1728313